IMPACT OF WALL BOUNDARY CONDITIONS ON PASSIVE SCALARS IN COMPLEX TURBULENT FLOWS

F. Secchi
Institute of Fluid Mechanics
Karlsruhe Institute of Technology
Kaiserstrasse 10
francesco.secchi@kit.edu

D. Gatti
Institute of Fluid Mechanics
Karlsruhe Institute of Technology
Kaiserstrasse 10
davide.gatti@kit.edu

B. Frohnapfel
Institute of Fluid Mechanics
Karlsruhe Institute of Technology
Kaiserstrasse 10
bettina.frohnapfel@kit.edu

ABSTRACT

This study presents the direct numerical simulation of two incompressible turbulent jets impinging on a solid surface. The two jets originate from two parallel ducts of square cross section where a fully developed turbulent flow is maintained. Several passive scalar fields are resolved within the simulation, as it is commonly done for the inclusion of a temperature field or concentration of chemical species in the flow. Transport and diffusion of scalar fields in the near-wall impingement region is influenced by the diffusion coefficient and the specific boundary condition assigned to each scalar field at the wall. The study reveals the far-off the wall areas in which effects of wall boundary conditions are noticeable on the mean distribution of each scalar field.

INTRODUCTION

It is not uncommon that state-of-art turbulence closure models fail to predict important flow features when applied to flow configurations of practical engineering interest. In this respect, turbulent jet impingement on solid walls is a well-known example (Dewan *et al.*, 2012; Zuckerman and Lior, 2005; Dairay *et al.*, 2014). While the study of an isolated impinging jet is instructive for understanding the physical mechanisms at play in the near-wall heat transfer process (Dairay *et al.*, 2015), most practical applications exploit arrays of several jets arranged in various geometrical layouts (Viskanta, 1993). The existence of multiple jets complicates greatly the resulting mean flow field and, thus, further extends the challenge of reproducing such complex flow features using RANS or even LES frameworks (Geers *et al.*, 2008; Thielen *et al.*, 2003; Draksler *et al.*, 2019).

The impingement of an isolated jet generates a wall jet that develops along the impingement plate. When multiple impinging jets are considered, the interaction between the wall jets produced by the multitude of the impinging jets can provoke a drastic modification of the resulting flow field. In such a case, many factors and geometrical parameters govern the development of the flow and are decisive in determining the for-mation of flow structures. For instance, the shape of the cross section of the jets nozzles, the Reynolds number in the jets, the spacing between the jets axes, the nozzles-to-plate distance and the presence of a cross-flow are known to cause the onset of different flow characteristics (Geers, 2004). For a broad range of parameters, studies in the literature show the formation of a *fountain flow* as a product of the interaction of the wall jets of two sufficiently close impinging jets (Barata, 1996; Geers *et al.*, 2001; Thielen *et al.*, 2003). The fountain flow consists of the upward directed flow generated by the interaction of two opposite directed wall jets. If the distance between the free jets axes is sufficiently small, the fountain flow can interact with the downward directed flow of the two jets with the consequent formation of an extended recirculating region consisting of two large counter rotating vortical structures.

Evidently, the presence of recirculating regions can affects mass, momentum and heat transfer features in the impingement region of the flow with alterations noticeable in the near wall region and, possibly, up to large wall normal distances.

Using a direct numerical simulation (DNS), the present work investigates a complex jet impingement configuration where two parallel square ducts are used to generate two incompressible turbulent jets that impinge on a flat solid wall. The layout considered in the study allows the realization of mean flow features characteristic of jet array configurations, or of complex flow scenarios which include recirculation effects due to flow impingement. Several passive scalar fields are resolved within the simulation with the purpose of enlightening the influence that wall-boundary conditions and diffusion properties associated to a particular scalar field have on the global evolution of the scalar quantity. This is relevant to understand whether or not the behavior of temperature and concentration scalars that can experience different wall boundary conditions can be modelled through analogy assumptions (Na and Hanratty, 2000).

Even though only incompressible and non-reacting flow is considered, the idealized setup represents a playground useful for the statistical assessment of passive scalar and velocity
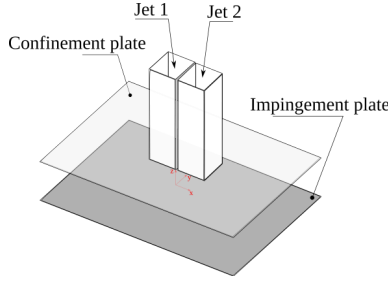
Figure 1. Sketch of the flow configuration.

fields, thus providing a rich data-set valuable for the development and testing of turbulence closure models of interest.

FLOW CONFIGURATION

The investigated flow configuration is sketched in figure 1. The turbulent jets originate form two parallel ducts of square cross section through which a fully developed turbulent flow is maintained. From the computational perspective, such inflow boundary condition for the jets is realized by performing a precursor simulation of two fully developed turbulent duct flows at constant flow rate where periodic boundary conditions are applied in the streamwise direction. The two ducts are separated by an interface of finite thickness $h \approx 0.03D$ and the impingement plate is located at a distance of $2D$ from the jets exit section. Here D represents the side length of the cross section of a duct. The flow is governed by the incompressible Navier-Stokes equations:

$$\frac{\partial u_j}{\partial x_j} = 0 \qquad (1)$$

$$\frac{\partial u_i}{\partial t} + u_j \frac{\partial u_i}{\partial x_j} = -\frac{\partial p}{\partial x_i} + \frac{1}{Re} \frac{\partial^2 u_i}{\partial x_j \partial x_j} \qquad (2)$$

where u_i, x_i, t and p represent, respectively, the ith fluid velocity component, the ith coordinate direction, the time and the pressure (the equations are valid for $(i, j = 1, 2, 3)$ and summation over repeated indices is implied). Equations 1 and 2 are made dimensionless using the mean bulk velocity U_b in the ducts and the length D. The Reynolds number is $Re = U_b D / \nu = 10\,000$, where ν indicates the kinematic viscosity of the fluid.

$N = 5$ passive scalar fields are resolved within the simulation through the numerical integration of transport-diffusion equations:

$$\frac{\partial \phi_k}{\partial t} + u_j \frac{\partial \phi_k}{\partial x_j} = \frac{1}{Pe} \frac{\partial^2 \phi_k}{\partial x_j \partial x_j} \qquad (3)$$

In equation 3, ϕ_k denotes the kth passive scalar field ($k = 1, ..., N$), and Pe denotes the Peclet number. Hence, the ratio Pe/Re corresponds to the Schmidt or Prandtl number for a concentration or temperature scalar, respectively. The parameters of the simulated scalar fields are collected in table 1.

NUMERICAL METHOD

The DNS is performed using the flow solver `Nek5000` (Fisher *et al.*, 2008-2021) which is based on the spectral element method (SEM) of Maday and Patera (1989) and allows

Table 1. Passive scalar fields parameters. Columns "Jet 1" and "Jet 2" refer to block-profile inflow boundary conditions applied to the two jets. D and N represent Dirichlet and Neumann boundary conditions respectively.

ϕ_i	Jet 1	Jet 2	Wall BC	Pe/Re
ϕ_1	0	1	$\phi = 0 \quad (D)$	1
ϕ_2	0	1	$\phi_{,n} = 0 \ (N)$	1
ϕ_3	1	0	$\phi_{,n} = 0 \ (N)$	1
ϕ_4	0	1	$\phi = 0 \quad (D)$	0.5
ϕ_5	0	1	$\phi_{,n} = 0 \ (N)$	0.5

to retain very high order spectral accuracy in the solution. In the context of the SEM, the governing equations are first recast in their weak form. Then, the discretisation of the functional space of the solution and the test functions is achieved through the classical Galerkin approximation. In the present work, the $\mathbb{P}_N - \mathbb{P}_N$ formulation is used. Within this framework, N^{th}-order Lagrange polynomials interpolants on Gauss-Lobatto-Legendre (GLL) quadrature nodes are used to approximate both the velocity and pressure spaces. Time integration of the discretized equations is performed using an implicit-explicit scheme (BDFk-EXTk, backward differencing and extrapolation of order $k = 3$). In particular, the linear terms are treated implicitly, while non-linear terms are treated explicitly. Over-integration is used for the dealiasing of the non-linear terms. At each time-step, the discretized problem is split into one Poisson problem for the pressure and one Helmholtz system for the velocity.

In the framework of `Nek5000`, equations 1, 2 and 3 are integrated numerically within a Cartesian coordinate system ($x = x_1$, $y = x_2$, $z = x_3$). The absence of statistically homogeneous directions in the flow configuration only allows the acquisition of time averages of flow variables. Results shown in the present work have been averaged in time for approximately $60D/U_b$. Further acquisition of data did not produce sensible changes in the computed statistics; in particular, a difference of less than 3% was observed in the peak values of the u_x velocity component in the $x - z$ plane at any x location. In the subsequent sections of this work, an over-line $\overline{(\cdot)}$ will be used to denote time averaging, while a prime superscript $(\cdot)'$ will indicate the fluctuations.

The computational meshes for the jets and the precursor ducts domains consist of, respectively, $\approx 3.86 \cdot 10^6$ and $\approx 0.93 \cdot 10^6$ elements. A grid independence study of the results has been performed by varying the polynomial order used for the representation of the solution. The largest discrepancies between the 3rd and the 5th order solutions were observed in the mean velocity field at large distances from the jet axes (*i.e.* $| x/D | \geq 6$). At these locations, the deviation of the computed maximum u_x velocity component on the $x - z$ plane amounted to approximately 6%. Nonetheless, in the region of interest of the flow, *i.e.* $-4 \leq x/D, y/D \leq 4$, the greatest discrepancies in the mean u_x velocity component between the two order solutions amounted up to less than 2%. The results presented in this work show the 5th polynomial order solution.

RESULTS
Mean velocity field

Mean x and z velocity components distributions in the plane $y/D = 0$ are reported in figure 2. Streamlines depicted in the figure evidence the formation of a large recirculating bubble consisting of two counter-rotating vortical structures between the two jets. The depicted flow structure is consistent with numerical and experimental findings of arrays of impinging jets (Geers *et al.*, 2004, 2006), even though in the present case the small spacing between the two jets sets off a much more visible recirculating zone. The latter is formed after the impingement of high momentum fluid coming from the two parallel free jets. The impingement deflects the two jets in two opposing directions and the subsequent interaction of the two deflected jets produces a strong upward directed flow. The upward motion of the fluid is strongly damped by the downward directed free jets and, ultimately, the fluid gets entrained back to move toward the impingement plate. The resulting mean flow consists of the two large counter rotating vortical structures observed in figure 2.

The recirculating region of the flow is also characterized by strong turbulence intensities relative to other regions of the flow. The distribution of the turbulent kinetic energy $0.5(\overline{u_x'^2} + \overline{u_y'^2} + \overline{u_z'^2})$ in the plane $y/D = 0$ is shown in figure 3. The turbulent kinetic energy reaches its maximum value in the recirculating region and has a secondary peak located very close to the wall at $x/D = 0$. The free shear layers of the free jets, the mixing layer between the jets and the outer shear layers developed along the impingement plate show values of the turbulent kinetic energy that are roughly 50% of the maximum values of the turbulent kinetic energy reached in the recirculating region.

The presence of the recirculating region has significant effects on the structure of the flow. Because of the bulging induced by the two vortical structures, the free jets are inclined towards opposing directions and their mean axes are not parallel anymore near the impingement region. Consequently, the location of the stagnation points on the impingement plate is not placed at the intersection of the free-stream jets axes with the impingement plate, but it is shifted slightly outwards. Selected contour lines of the pressure field in the near impingement region are reported in figure 4. In the same figure, two black dashed lines represent the axes of the two undisturbed jets. It is clear from the figure that the maxima of the pressure field, which correspond to the locations of the two stagnation points, are not located exactly underneath the jets axes, but they are slightly shifted toward the outside region.

The development of the flow towards the positive and negative x directions does not appear to be significantly affected by the recirculating region. On both sides of the two jets, the deflection of the flow produces a wall-parallel flow that has characteristics very similar to those of three-dimensional wall jets (Kakka and Anupindi, 2021). Selected contour lines of the $\overline{u_x}$ velocity component in the $y - z$ planes at $x/D = 1, 2, 3$ are reported in figure 5. It can be seen that, as the flow develops in the downstream direction, the wall jet spreads in the y direction, while the region of maximum velocity gets flattened. Naturally, a symmetric behavior is observed for the development of the flow in the negative x direction. On the other hand, the wall jet that develops in the y direction after the jets impingement is significantly affected by the recirculating region that exists between the two jets. Selected contour lines of the $\overline{u_y}$ velocity component in $x - z$ planes at $y/D = 1, 2, 3$ are displayed in figure 6. The contour lines evidence a bulging region of high speed fluid located far away from the wall (*i.e.*
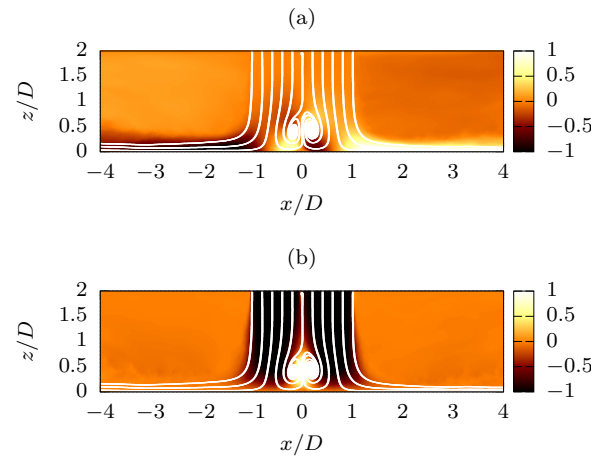

Figure 2. Time averaged mean velocity distribution in the plane $y/D = 0$. (a) $\overline{u_x}/U_b$ velocity component; (b) $\overline{u_z}/U_b$ velocity component. White lines represent streamlines.
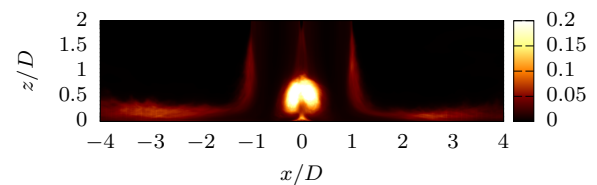

Figure 3. Time averaged turbulent kinetic energy in the plane $y/D = 0$.
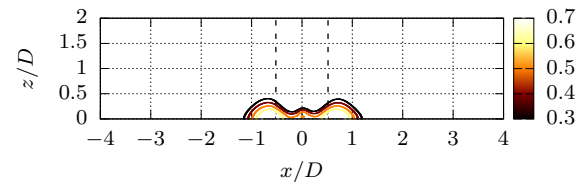

Figure 4. Time averaged contour lines of constant pressure in the plane $y/D = 0$. Black dashed lines represent the jets axes.

$z/D \approx 1$ at $x/D = 0$. For increasing y distances, this region of high speed fluid has the tendency to detach from the underlying developing three dimensional wall jet.

Passive scalar fields

The recirculating region between the two jets has a profound impact on the structure of the mean flow and, consequently, it is expected to affect also the mean distribution of passive scalar fields. As a primary effect, the recirculating flow produces an intense upward motion in the near wall impingement region close to $x/D, y/D = 0$. In this portion of the domain, the upward directed flow can advect the boundary-condition-informed passive scalar field away from the wall and, in this sense, spread the information of wall boundary conditions at large distances from the wall. The spiralling pattern followed by fluid particles entangled in the recirculating
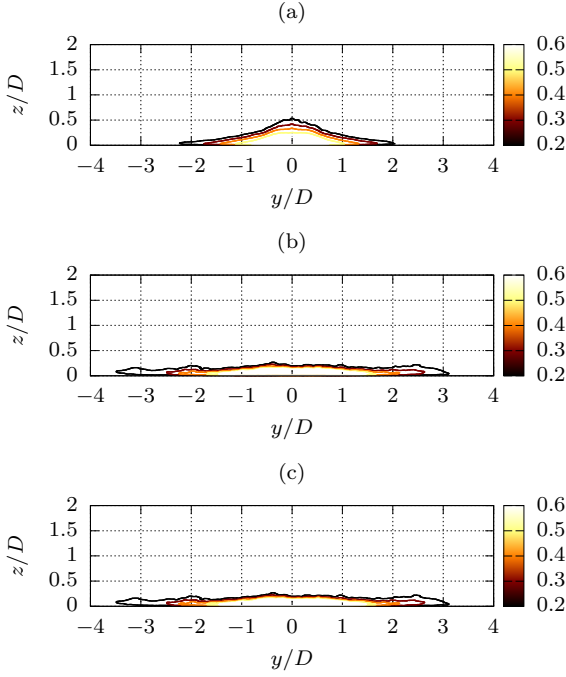
Figure 5. Time averaged contour lines of the velocity component $\overline{u_x}/U_b$. (a) plane $y/D = 1$; (b) plane $y/D = 2$; (c) plane $y/D = 3$.

Figure 6. Time averaged contour lines of the velocity component $\overline{u_y}/U_b$. (a) plane $x/D = 1$; (b) plane $x/D = 2$; (c) plane $x/D = 3$.

region of the flow and the high turbulence intensities observed in this region are also expected to strongly influence the local advection and diffusion of passive scalar fields.

To address these points, several passive scalar fields have been included in the DNS. Each simulated scalar field differs from the others because of the prescribed inflow and wall boundary conditions and diffusivity properties. The parameters assigned to all the simulated scalar fields are reported in table 1. In all cases, the inflow profile consists of a uniform distribution on the exit section of a jet. For each scalar field, the constant is set equal to 1 on one jet and 0 on the other. The columns "Jet 1" and "Jet 2" in table 1 refer to the inflow profiles assigned to each scalar field. An example of time averaged distributions of passive scalar fields ϕ_1 and ϕ_3 in the $x-z$ plane at $y/D = 0$ is displayed in figure 7.

Sampling of data during the simulation at specific locations provides with time-resolved data useful for assessing the influence of wall boundary conditions and diffusivity properties on the evolution of passive scalars. Scatter plots of three different scalar pairs are reported in figure 8 for data sampled at $x/D = 0.022$, $y/D = 0$, $z/D = 0.002$ (refer to table 1 for numbering of the scalar fields and respective parameters). In each panel of the figure, a curve represents the ensemble average of the data on equispaced discrete bins of the horizontal axis. In addition, the curve is color-coded according to the probability of occurrence of data within a certain discrete bin.

The pair (ϕ_2, ϕ_3) represents a reference case since both the scalars are characterized by same Peclet number and wall boundary conditions. For such a combination, the linear behaviour depicted in figure 8(a) is expected. Indeed, despite the different inflow bounary conditions, the two fields are characterized by exactly the same mean distribution. Deviations from the straight line of the reference case are observed whenever a
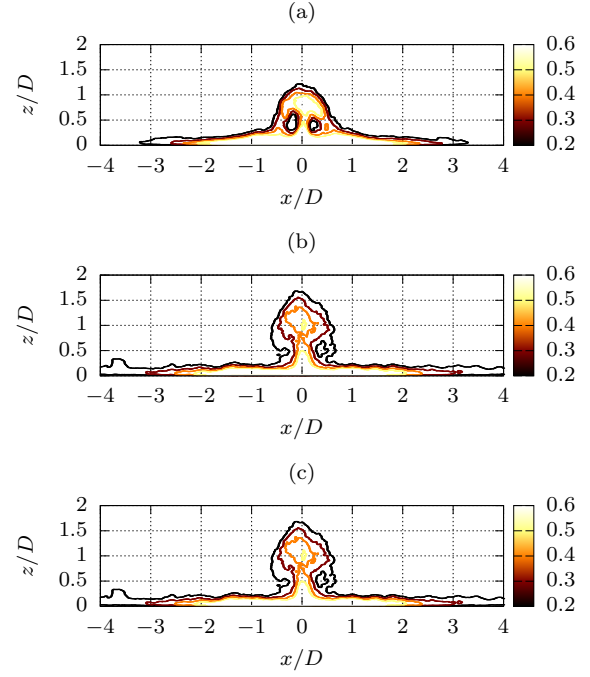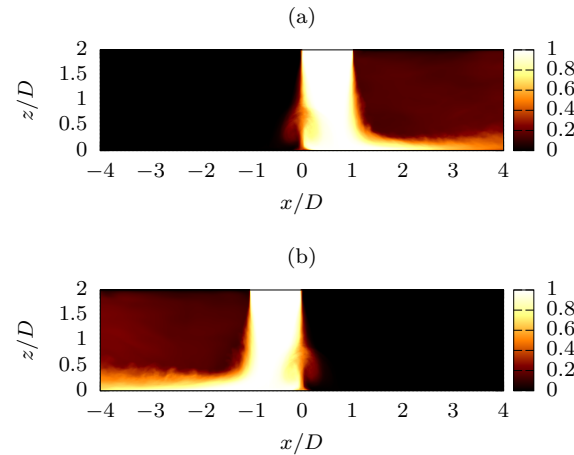

Figure 7. Time averaged distribution of passive scalar fields in the plane $y/D = 0$. (a) ϕ_1; (b) ϕ_3.

change in either wall boundary conditions or Peclet number occurs. For instance, the effect of decreasing the Peclet number for one of the two scalar fields can be pictured in figure 8(b). In this case, by comparison with figure 8(a), a broader scatter characterizes the scalar field ϕ_5 for any given value of ϕ_2. Note that ϕ_5 differs from ϕ_3 only because of a smaller Peclet number; hence, the greater scatter of data observed must be associated to the stronger diffusion that characterizes the scalar field ϕ_5 with respect to the scalar ϕ_3. Nonetheless, averaging over the sampled data evidences a mean behavior very similar to the one observed for the pair (ϕ_2, ϕ_3).

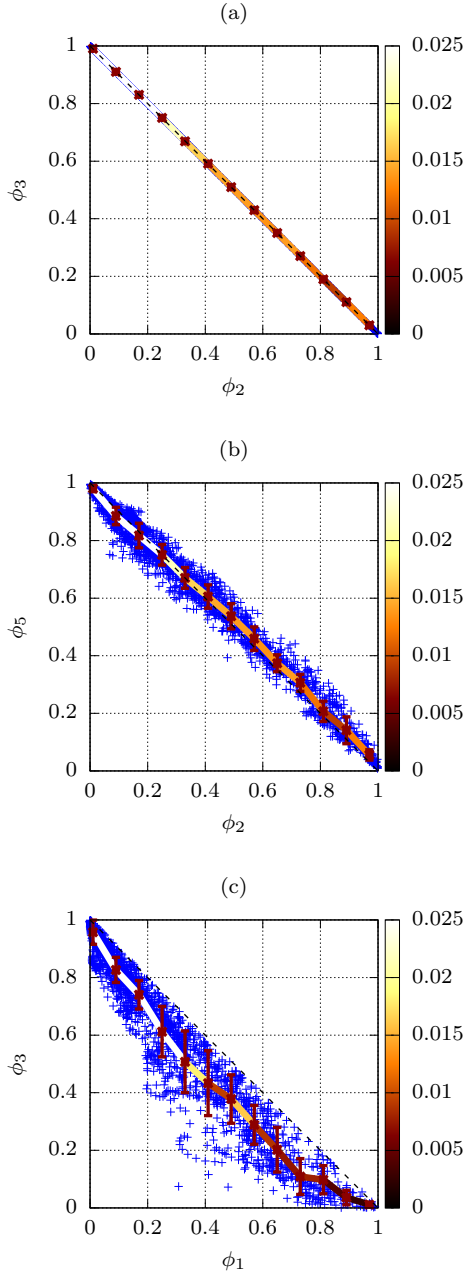Similarly, the effect of varying the wall boundary condi-

4

Figure 8. Scatter plots of passive scalar fields at $x/D = 0.022$, $y/D = 0$, $z/D = 0$. $\mathbf{+\,+\,+}$, sampled values. The mean over the ensemble of sampled values is depicted by a solid line in each plot and it is color-coded according to the probability associated to the realization of events of the scalar fields in the considered range of values. Error bars represent one standard deviation interval.

tion for one of the two considered fields can be envisaged by the comparison of figures 8(a) and (c). Because of the zero Dirichlet boundary condition, non-zero flux through the wall can occur to the scalar ϕ_1 at the wall, thus influencing the values of the scalar in the near-wall region. In the particular case considered, an outward flux at the wall determines the occurrence of lower values of the field ϕ_1 in the near-wall region when compared to values of ϕ_2 at the same locations. As a result, the deviation from the linear behaviour observed in figure
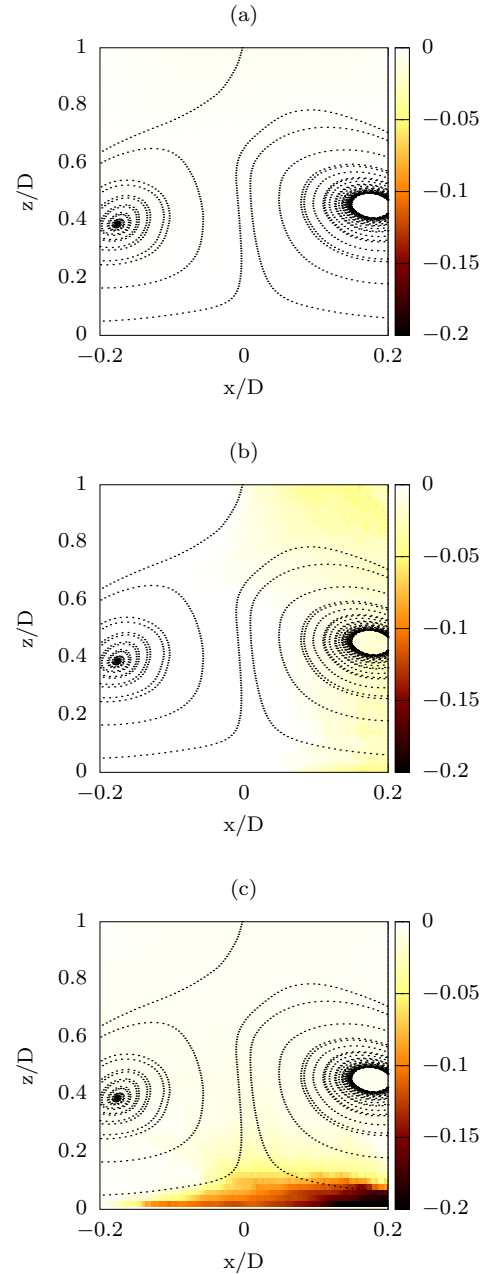

Figure 9. Color maps of the parameter δ representing the deviation from the "linear" behaviour displayed by the scatter plots at a given location in space. The panels represent the scalar field pairs: (a) (ϕ_2, ϕ_3); (b) (ϕ_2, ϕ_5); (c) (ϕ_1, ϕ_3). Streamlines are also depicted by black lines to identify the location of the recirculating region.

8(c) can be interpreted.

At a given location, a quantitative measure of the departure from the linear relation occurring between two passive scalars can be identified through the parameter δ, which is defined as:

$$\delta = \int_0^1 \left[\langle \phi_i(s) \rangle - (1-s) \right] \mathrm{d}s \qquad (4)$$

In the equation, $\langle \cdot \rangle$ indicates the ensemble average operator.

5

Hence, δ represents the signed area between the straight line $\phi = 1 - s$ and the curve of the ensemble averaged values of the data on discrete bins.

Color maps of the distribution of δ in the impingement region are reported in figure 9 for the same passive scalar pairs considered before. While for the pair (ϕ_2, ϕ_3) δ is zero everywhere (figure 9(a)), regions where evident departure from the linear behaviour are easily identified for the scalar pairs (ϕ_2, ϕ_5) and (ϕ_1, ϕ_3) in figure 9(b) and (c) respectively. It is observed that the largest deviations from the reference linear behavior occur for the case of variation of wall boundary condition from zero flux to homogeneous Dirichlet. In this respect, the color map of figure 9(c) carries the information about the region of the flow that is directly affected by such a change of wall boundary condition in one of the scalar fields.

CONCLUSIONS

This work presents the DNS of two parallel square turbulent jets impinging on a flat solid wall. The study considers an incompressible flow of a Newtonian fluid with constant properties and in the absence of external volume forces. Several passive scalar fields were simulated in order to investigate the effect that wall boundary conditions and diffusivity parameter have on the global mean distribution of the scalar fields.

The study shows that the examined flow configuration produces a very complex mean flow field which includes two large counter-rotating vortical structures in between the two jets in the impingement region. The presence of such structures has profound effects on the overall structure of the mean flow field and, ultimately, on the mean distribution of the passive scalar fields. Deviations from a reference distribution of two scalar fields shows the effects of varying diffusivity properties and wall boundary conditions in one of the considered scalar fields. The largest deviations are associated to a variation of wall boundary conditions and the effects of such a change are felt up to $z/D \approx 0.1$. In particular, this extended region of influence of wall boundary conditions is linked to the continuous upward fluid motion generated by the presence of the two counter-rotating vortical structures between the two jets.

ACKNOWLEDGEMENTS

REFERENCES

Barata, J.M.M. 1996 Fountain flows produced by multiple impinging jets in a crossflow. *AIAA Journal* **34** (12), 2523–2530.

Dairay, F., Fortuné, V., Lamballais, E. & Brizzi, L. E. 2015 Direct numerical simulation of a turbulent jet impinging on a heated wall. *J. Fluid Mech.* **764**, 362–394.

Dairay, T., Fortuné, V., Lamballais, E. & Brizzi, L.E. 2014 Les of a turbulent jet impinging on a heated wall using high-order numerical schemes. *Int. J. of Heat and Fluid Flow* **50**, 177–187.

Dewan, A., Dutta, R. & Srinivasan, B. 2012 Recent trends in computation of turbulent jet impingement heat transfer. *Heat Transfer Engineering* **33** (4-5), 447–460.

Draksler, M., Končar, B. & Cizelj, L. 2019 On the accuracy of large eddy simulation of multiple impinging jets. *International Journal of Heat and Mass Transfer* **133**, 596–605.

Fisher, P. F., Lottes, J. W. & Kerkemeier, S. G. 2008-2021 NEK5000 v19.0. http://nek5000.mcs.anl.gov/ Argonne National Laboratory, Illinois.

Geers, L.F.G. 2004 Multiple impinging jet arrays: an experimental study on flow and heat transfer. PhD thesis, Technische Universiteit Delft.

Geers, L.F.G., Hanjalić, K. & Tummers, M. J. 2006 Wall imprint of turbulent structures and heat transfer in multiple impinging jet arrays. *J. of Fluid Mech.* **546**, 255–284.

Geers, L.F.G., Tummers, M.J., Bueninck, T.J. & Hanjalić, K. 2008 Heat transfer correlation for hexagonal and in-line arrays of impinging jets. *Int. J. of Heat and Mass Transfer* **51** (21), 5389–5399.

Geers, L.F.G., Tummers, M.J. & Hanjalić, K. 2001 PIV measurements in impinging jets at a high reynolds number. In *Proc. Second Int. Symposium on Turbulence and Shear Flow Phenomena.* (ed. E Lindborg et al.), pp. 289–295.

Geers, L.F.G., Tummers, M.J. & Hanjalić, K. 2004 Experimental investigation of impinging jet arrays. *Experiments in Fluids* **36**, 946–958.

Kakka, P. & Anupindi, K. 2021 Flow and thermal characteristics of three-dimensional turbulent wall jet. *Physics of Fluids* **33** (2), 025108.

Maday, Y. & Patera, A.T. 1989 Spectral element methods for the incompressible Navier-Stokes equations. In *State of the art surveys on computational mechanics ASME*, pp. 71–143.

Na, Y. & Hanratty, T.J. 2000 Limiting behavior of turbulent scalar transport close to a wall. *International Journal of Heat and Mass Transfer* **43** (10), 1749–1758.

Thielen, L., Jonker, H.J.J. & Hanjalić, K. 2003 Symmetry breaking of flow and heat transfer in multiple impinging jets. *Int. J. of Heat and Fluid Flow* **24** (4), 444–453.

Viskanta, R. 1993 Heat transfer to impinging isothermal gas and flame jets. *Experimental Thermal and Fluid Science* **6** (2), 111–134.

Zuckerman, N. & Lior, N. 2005 Impingement Heat Transfer: Correlations and Numerical Modeling. *Journal of Heat Transfer* **127** (5), 544–552.